Indian Journal of Advances in Chemical Science

Research Article

Structural Evaluation, Equilibrium Studies, Binding Affinity and Antioxidant Properties; Antimicrobial and Cytotoxicity Assay of Novel Hydrazone with Nitrophenyl and Isonicotinoyl N-Oxide Moieties and Its 3d- Metal Complexes

Anitha Nayakini[1]*, Samala Deepa[1], Sudeepa Kunche[3], Ch. Sarala Devi[1]*

[1]Department of Chemistry, Osmania University, Hyderabad, Telangana, India, [2]Department of Chemistry, Nizam College, Basherbagh, Osmania University, Hyderabad, Telangana, India

ABSTRACT

A novel isonicotinoyl N-oxide hydrazone and its cobalt, nickel, copper, and zinc metal complexes are characterized and their *in vitro* biological activity is explored. pH metric studies were performed in a 40% DMF-H_2O medium to calculate the pKa values of the ligand under investigation to ascertain its basicity. HyerChem7.5 software was used to deduce contour maps of frontier orbitals HOMO and LUMO of title ligand to identify donor sites probability in forming metal complexes. The title hydrazone and its newly prepared metal complexes were evaluated for structural analysis by various spectroanalytical tools, namely, FT-IR, ^{1}H-NMR, ESI-Mass, UV-Vis, TGA&DTA, SEM-EDX, and ESR. The complexes are assigned octahedral geometry with 1:2 (M[II]: Ligand) composition wherein two ligand moieties are coordinated through O^- and N donor sites and with two coordinated water molecules. The synthesized compounds were investigated for DNA binding interactions with CT-DNA absorption and fluorescence techniques. The screening for antioxidant activity of all compounds was assessed with a DPPH radical scavenging assay. Antibacterial and antifungal studies conducted with all title compounds were helpful to evaluate their relative potential activities. The synthesized compounds tested against cell lines (MCF-7), for cytotoxic activity by adopting MTT assay is assertive to understand relatively their active property.

Key words: Antimicrobial, Antioxidant, Contour maps, Cytotoxicity, DNA binding, Equilibrium studies.

1. INTRODUCTION

There is a constant requirement for research to discover new pharmaceuticals to combat infectious, non-infectious, and autoimmune diseases. Scientists began their search for new drug compounds with high efficacy and fewer side effects [1]. As there is a persistent need for various disease-fighting chemicals to be discovered, researchers have been working to design and synthesize new chemical substances with the ability to target against various diseases [2]. Hydrazones and carboxy hydrazone compounds with various heterocyclic moieties through their unique biological action and excellent coordination ability with metal ions have become potential topics in pharmaceutical research [3, 4]. The coordination properties of carboxy hydrazones are influenced by reaction conditions and the nature of substituents [5]. Because of their adaptability, carboxy hydrazones are efficient bidentate, tridentate, or polydentate chelating moieties, that may bind to a wide range of transition metal ions to form complexes prone to potent biological activities [6].

The hydrazones play an important role in improving drug delivery at specific site, including areas such as tumor tissue and thrombosis [7]. Hydrazones with their prospective in modification of drugs have been generally used in cancer treatments [8]. For example, the drug doxorubicin (DOX), is conjugated with hydrazones to avoid toxic effects, and consequently to increase survival rates [9, 10]. The tenability of hydrazones and difference in the chemical composition of drug conjugates enable wide applications in addressing various types of cancers [11]. The imine bond is responsible in hydrazones that allow for the release of drugs at the targeted site [12]. Such type of target-viewed action is vital for appropriate drug functionality and in restraining toxic effects. Hydrazones are used currently to promote in drug delivery at required site in the treatment of cancer, inflammatory diseases, and in the inhibition of platelet accumulation [13]. The outcome of these advances in research is contributory in corresponding applications [14]. The use of hydrazones is anticipated for better treatment of disease and decreasing excess toxicity from harsh therapeutics [15].

A review of the literature on isonicotinoyl hydrazones reveals that these compounds are suitable as therapeutic agents with their reasonable efficiency and lesser toxicity, and also their activities are enhanced upon binding with transition metals [16]. Popiołek *et al.* [17] synthesized and determined the experimental lipophilicity of hydrazide-hydrazones of isonicotinic acid. These compounds were tested *in vitro* against reference strains of bacteria and fungi wherein some of these hydrazide-hydrazones were notified as considerably more efficient.

Corresponding authors:
Ch. Sarala Devi,
E-mail: prof.saraladevi.ch@gmail.com

ISSN NO: 2320-0898 (p); 2320-0928 (e)
DOI: 10.22607/IJACS.2025.1302006

Received: 06th February, 2025;
Revised: 06th March, 2025;
Accepted: 13th March, 2025
Published: 02nd May, 2025

Isonicotinoyl hydrazone of pyridoxal is a tridentate O^-, N, O^- donor base which showed promising results in chelation therapy. The positive aspects of this hydrazone are; its economical synthesis, oral effectiveness, non-toxic nature, and more affinity to bind with Iron [18]. Several recent articles have summarized the biological activities of the metal chelates of hydrazone scaffolds with heterocyclic moieties in exhibiting antimicrobial, anti-inflammatory, anticancer, antioxidant, and antiprotozoal properties [19].

Platinum metal complexes, such as carboplatin and oxaliplatin which emerged as successful anticancer drugs inspired researchers to work on other transition metal complexes also, with a special focus on 3d-metal ions [20]. One of the important 3d metal complexes that were considered for clinical trials was Co(III) schiff base complex, namely, Doxovir, which is proved active against simplex virus1, drug-resistant herpes. It has been stated that the promising antiviral activity of Doxovir is due to the direct interaction of complex with proteins associated in viral infiltration [21, 22]. The interaction of non-steroidal anti-inflammatory drugs with Cu(II) reveals the formation of corresponding copper complexes that would result a decrease in gastrointestinal toxicity, andcan cause improvement in anti-inflammatory and antiulcerogenic activities [23]. Chemotherapeutic properties of various copper-based complexes were also reported [24]. Many copper metal chelates were known for cytotoxic activity through cell apoptosis and enzyme inhibition [25]. Many zinc complexes have gained more consideration as anticancer drugs due to less toxicity [26].

Keeping in view, the biological activity of 3d metal complexes and of various hydrazone compounds with a special focus on isonicotinic acid hydrazone derivatives of clinical relevance as mentioned above, we planned herein synthesis and structural evaluation of Isonicotinoyl N-oxide hydrazine, namely, 4-(2-(4-nitrobenzylidene) hydrazinecarbonyl)pyridine1-oxide and its cobalt, nickel, copper, and zinc metal complexes to understand their structural features, free radical scavenging properties, ability to bind with CT-DNA, and *in vitro* antimicrobial and *in vitro* antiproliferative activities.

2. EXPERIMENTAL SECTION

2.1 Materials and Methods

The supporting file covers the various chemical materials and instrumental details, the mathematical expressions used in the calculations of pH-metric equilibrium studies, and all other information related to characterization. It also covers experimental methods of DNA binding affinity, free radical scavenging potential, antimicrobial efficacy, and cytotoxicity studies.

2.1.1. Synthesis of hydrazone (HL)

Synthesis of 4-(2-(4-nitrobenzylidene)hydrazinecarbonyl)pyridine1-oxide (HL) involves four steps. The first step deals with the preparation of 4-carboxypyridine1-oxide, the second step with the preparation of 4-(methoxycarbonyl) pyridine1-oxide, the third step with a synthesis of 4-(hydrazine carbonyl) pyridine1-oxide, and the fourth step with the preparation of 4-(2-(4-nitrobenzylidene) hydrazinecarbonyl) pyridine1-oxide (HL). Synthetic procedure methods for the first three steps are provided in the supporting file and the fourth step synthesis is given below.

2.1.2. Synthesis of 4-(2-(4-nitrobenzylidene)hydrazinecarbonyl) pyridine1-oxide (HL) [Scheme-I]

4-nitrobenzaldehyde (1.51 g, 15 mmol) in ethanol (40 mL) was subjected to stirring on a magnetic stirrer at room temperature for 30–40 min. In hot ethanol (40 mL), the synthesized 4-(hydrazine carbonyl) pyridine1-oxide (1.53 g, 15 mmol) was dissolved and then slowly introduced drop-wise while stirring the mixture. These were then refluxed for 4 h at 60–70°C on a magnetic stirrer, and the reaction progression was assessed by testing on thin layer chromatographic plates. Finally, the product obtained was washed with ethanol to remove impurities and then subjected to the process of recrystallization to obtain the title ligand as a pure light yellow colored amorphous solid.

Data of analysis: Yield: 87.5%; Physical state: solid; Color: light yellow; M.pt: 267°C; Calcd (%) of $C_{13}H_{10}N_4O_4$: C, 54.55; H, 3.52; N, 19.57; O, 22.36; Observed (%): C, 54.49; H, 3.55; N, 19.60; O, 22.45; ^{1}H-NMR (400 MHz, δppm, DMSO-d_6): 12.23 (s, 1H, NH-CO), 8.46 (s, 1H, N=CH), 8.31 (d, 2H, Py-H), 7.85 (d, 2H, Py-H), 8.24 (d, 2H, Ph-H), 7.94 (d, 2H, Ph-H); ^{13}C-NMR (100 MHz, δppm, DMSO-d_6): 160.95 (C=O), 159.44, 131.10, 110.46, 107.80, 102.59 (Ph-C), 139.10, 128.21, 125.03 (Py-C), 149.49 (CH=N); FT-IR (KBr, υ/cm^{-1}): 3333 & 3190 υ(N-H), 3072–2843 υ(Ar-CH), 1677 υ(C=O), 1572 υ(C=N), 1514–1487 υ(C=N & C=C), 1340 υ(C-N), 1239 υ(C-O); ESI-Mass-positve mode (m/z, amu): 287.0781 $[M+1]^+$; UV-Vis (λ_{max}, nm, DMSO): 255 & 346 (π→π* & n→π*).

2.1.3. Synthesis of metal complexes [Scheme-II]

Metal complexes of cobalt, nickel, copper, and zinc were prepared by mixing the respective metal chloride salt (10 mmol) in ethanol and DMF-ethanolic suspension of ligand (20 mmol) in a 1:2 molar ratio to obtain the corresponding metal complex. The resultant solution was refluxed at 60°C for 6 h. Further pH of the mixture of the solution was maintained by the addition of few drops of ethanolic ammonia to facilitate the formation of complex through the dissociation of protons from the ligand. The obtained solid complexes were separated through filtration, washed with hot ethanol, and dried in a desiccator. The color of each complex observed is; for **Co(II) complex**-maroon, **Ni(II) complex**-orange, **Cu(II) complex**-dark green, and **Zn(II) complex**-orange yellow. Their purity was also confirmed by thin-layer chromatography.

2.1.3.1. Co(II) complex

Data of analysis: Yield: 85%; Physical state: solid; M.pt: >300°C; Calc (%) for $C_{26}H_{22}CoN_8O_{10}$: C, 46.93; H, 3.33; N, 16.84; O, 24.05; Co, 8.85; found (%): C, 46.91; H, 3.35; N, 16.87; O, 24.08; Co, 8.80; IR (υ/cm^{-1}, KBr): 3444 υ(H_2O), 3109–2831 υ(Ar-CH), 1586 and 1511 υ(C=N), 1363 υ(C-N), 1337 and 1217 υ(C-O), 419 υ (Co-O), 353 υ(Co-N); ESI-Mass-negative mode (amu, m/z): 664.0282 $[M-1]^-$; Electronic spectral peaks (λ_{max}, nm, DMSO): 257 (π→π*), 331 (n→π*), 500 and 730 (*d*→*d*); μ_{eff}: 4.38 B.M; Molar conductivity (DMSO, 10^{-3} M): 15.62 ohm^{-1} cm^2 mol^{-1}.

2.1.3.2. Ni(II) complex

Data of analysis: Yield: 89%; Physical state: solid; M.pt: >300°C; Calc (%) for $C_{26}H_{22}NiN_8O_{10}$: C, 46.94; H, 3.31; N, 16.85; O, 24.07; Ni, 8.83; found (%): C, 46.96; H, 3.34; N, 16.84; O, 24.05; Ni, 8.81; IR (υ/cm^{-1}, KBr): 3442 υ(H_2O), 3110–2842 υ(Ar-CH), 1516 υ(C=N), 1368 υ(C-N), 1341 & 1219 υ(C-O), 419 υ (Ni-O), 353 υ(Ni-N); ESI-Mass-negative mode (amu, m/z): 663.0245 $[M-2]^-$; Electronic spectral peaks (λ_{max}, nm, DMSO): 258 (π→π*), 326 (n→π*), 410, 593 & 699 (*d*→*d*); μ_{eff}: 2.82 B.M; Molar conductivity (DMSO, 10^{-3} M): 14.78 ohm^{-1} cm^2 mol^{-1}.

2.1.3.3. Cu(II) complex

Data of analysis: Yield: 86%; Physical state: solid; M.pt: >300°C; Calc (%) for $C_{26}H_{22}CuN_8O_{10}$: C, 46.60; H, 3.30; N, 16.73; O, 23.89; Cu, 9.48; found (%): C, 46.63; H, 3.32; N, 16.72; O, 23.90; Cu, 9.43; IR (υ/cm^{-1}, KBr): 3410 υ(H_2O), 3110–2845 υ(Ar-CH), 1597–1504 υ(C=N), 1367 υ(C-N), 1345 & 1256 υ(C-O), 582 υ (Cu-O), 407 υ(Cu-N); ESI-Mass-negative mode (amu, m/z): 593.1117 $[M-N_2O_3]^-$; Electronic spectral peaks (λ_{max}, nm, DMSO): 257 (π→π*), 328 (n→π*), 385 (CT), 473 (*d*→*d*); μ_{eff}: 1.73 B.M; Molar conductivity (DMSO, 10^{-3} M): 18.32 ohm^{-1} cm^2 mol^{-1}.

2.1.3.4. Zn(II) complex

Data of analysis: Yield: 85%; Physical state: solid; M.pt: >300°C; Calc (%) for $C_{26}H_{22}ZnN_8O_{10}$: C, 46.48; H, 3.29; N, 16.68; O, 23.82; Zn, 9.73; found (%): C, 46.52; H, 3.35; N, 16.58; O, 23.89; Zn, 9.66; IR (υ/cm^{-1}, KBr): 3440 υ(H_2O), 3109–2823 υ(Ar-CH), 1565 & 1511 υ(C=N), 1367 υ(C-N), 1348 &1248 υ(C-O), 579 υ (Zn-O), 354 υ(Zn-N); ESI-Mass-negative mode (amu, m/z): 668.2363 $[M-2]^-$; Electronic spectral peaks (λ_{max}, nm, DMSO): 261 (π→π*), 328 (n→π*), 409 (CT); μ_{eff}: 0 B.M; Molar conductivity (DMSO, 10^{-3} M): 14.63 ohm^{-1} cm^2 mol^{-1}.

2.2. Ligation Properties

2.2.1. Equilibrium studies

The coordination characteristics of the ligand (**HL**) and its interaction with 3d transition metal ions in 40% DMF-H_2O were examined in this work. The pKa value that correlates to the dissociation of proton in **HL** was calculated using the pH metric titration technique [27]. In addition, pH titrations were performed in the presence of Co(II), Ni(II), and Cu(II) metal ions in a 40% DMF-H_2O solvent medium at 303 K temperature while retaining 0.1M ionic strength. Using the Van Uitert and Hass equation, the recorded pH values in the above-aquo organic medium were corrected [28].

2.3. Frontier Orbital Properties

The present work employed the Hyperchem7.5 software to determine the ligand (**HL**) frontier molecular orbital characteristics. These frontier molecular orbitals contour maps are computed for optimized molecules using the PM3 method [29].

2.4. DNA Binding Studies

2.4.1. UV-visible absorption

The Tris-HCl buffer medium was used while performing absorption titrations to examine the interaction of the ligand and its metal complexes with CT-DNA. Titrations were carried out by adjusting the CT-DNA concentration (0–140 µM) while maintaining the title compound concentration at 140 µM. Corresponding absorption spectra were acquired following each incremental addition of CT-DNA solution (20 µM). The intrinsic binding constant (K_b) for all systems is calculated [30].

2.5. Fluorescence Quenching

By using a competitive fluorescence quenching experiment, the binding strength of each test compound with CT-DNA is also evaluated. The fluorescence titrations were conducted in Tris-HCl buffer solution by keeping the concentration of EB and CT-DNA and varying the quantity of the test substance [31]. The quenching constant (K_{sv}) and the binding constant (K_b) for each system are calculated by the equations given in the supporting file.

2.6. Antioxidant Activity by DPPH Assay

By using the DPPH (2,2-diphenyl-1-picrylhydrazyl) method, the antioxidant properties of ligand and metal complexes were evaluated. To 0.008% (w/v) DPPH in methanol taken in different flasks, a series of concentrations of all test systems and standard ascorbic acid solution were added and then kept in the dark for 30 min at room temperature. The absorbance of all systems after the incubation period was measured at 517 nm to calculate the percentage for radical scavenging [32].

2.7. Antibacterial Assay

The spread plate method was used to perform the antibacterial assay. *Staphylococcus* and *Bacillus* were selected as Gram-positive bacteria for the investigations, whereas *E. coli* and *Klebsiella* were selected as Gram-negative bacteria. The results were assessed in terms of the zone of inhibition after the bacterial plates were loaded with test substances and incubated for 18–24 h at 37°C.

2.8. Antifungal Assay

The media for potato dextrose agar and yeast extract peptone agar were made and autoclaved. Both Aspergillus and Candida were used in the antifungal assay. After loading each prepared fungal plate with 100 µL of samples, the plates were incubated for 96 h at 25°C. Following the period of incubation, the fungus plates were examined, and the results were reported in terms of the zone of inhibition.

2.9. MTT Assay

Human breast cancer cell lines MCF-7 were treated with the MTT salt and incubated for 1–4 h. The metabolically active cancer cell lines reduce the MTT salt, resulting in the production of formazan crystals which precipitate during the incubation period. In triplicate, different doses of the test substance were used to assess cell viability. The ability of cells to transform MTT into formazan is lost when they die in the presence of a potentially cytotoxic substance. By measuring the optical density of solubilized crystals in DMSO at 570 nm both before (control) and after treatment of cell lines with the test compound (treated), formazan can be quantified. The following formula was used to determine the percentage growth inhibition: % Inhibition = 100(Control-Treated)/Control [33].

3. RESULTS AND DISCUSSION

3.1. pH Metric Equilibrium Studies

The pKa of the ligand in solution can be achieved by performing pH-metric titrations at constant temperature and ionic strength. The titration curves of pH versus volume of NaOH added presented in Figure 2, and linear plots of pH versus log $[(1-\bar{n}_A)/\bar{n}_A]$ shown in Figure 3, indicate the dissociation of one proton. The pKa value of 9.20 evaluated from the data of the linear plot method is assignable to the ionization of a proton from carboxy hydrozyl nitrogen (pKa) through enolization. Further, the titrations were performed under the same conditions in the presence of metal ions. The titration curves clearly showed a lowering of pH due to the displacement of proton in the presence of metal ion indicating the formation of corresponding complexes in solution [34] Figure 2.

The observations noted in the above equilibrium studies confirm that the candidate ligand is a monoprotic system (**HL**), and also convey the inference to determine donor sites for metal binding. The ascribable

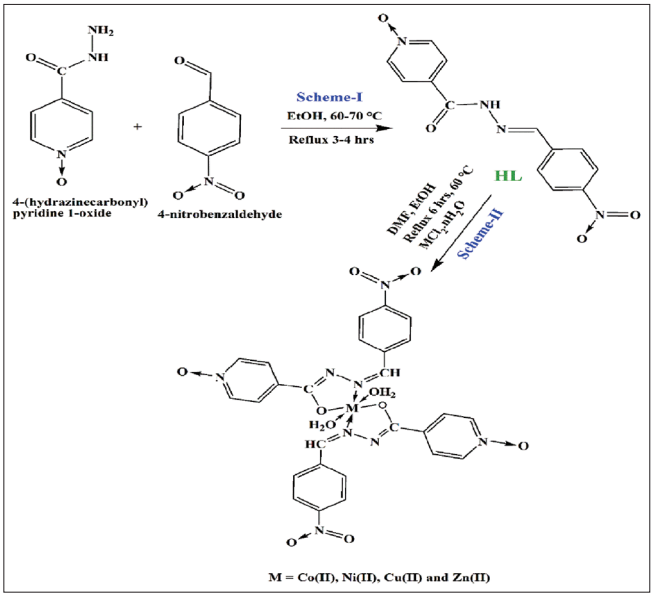

Figure 1: Synthetic route map for ligand and metal complexes.

donor sites of enolate **O**$^-$ and imine **N** indicate the bidentate nature of the title ligand.

3.2. Molecular Orbital Properties

To envision the properties of frontier orbitals, computational tools of HyperChem7.5 software were utilized to generate geometry-optimized structures of **HL** and L$^-$(ionized form), and presented in Figure 5. In depicted contour maps of HOMO, the orientation of these orbitals at presumed donor sites is very much evident both in molecular and ionized forms. As the dissociation of the proton is evident due to complex formation from pH-metric studies, based on the orientation of HOMO in ionized form, bonding modes ought to be enolate oxygen and imine nitrogen augmenting the results obtained from equilibrium studies. Further, the difference in energies of HOMO and LUMO which is observed as less in ionized form compared to molecular form infers the formation of more stable complexes involving ligand in dissociated form [31].

3.3. Characterization of Synthesized Compounds

All the newly prepared complexes are colored, stable, and have shown physical appearance of amorphous form. All these complexes are soluble in DMSO, and their non-electrolytic property is evident from molar conductivity measurements. The structural elucidation of hydrazone ligand and its derived 3d complexes is done by the analyses of recorded spectral and analytical data.

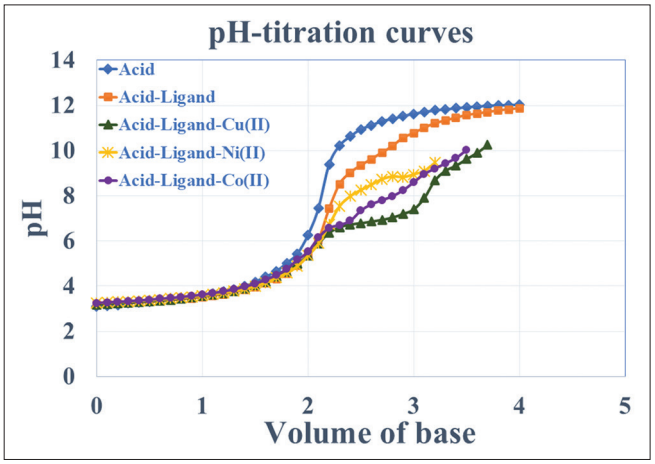

Figure 2: pH Titration curves in 40% DMF-water medium at 303K and 0.1M Ionic strength.

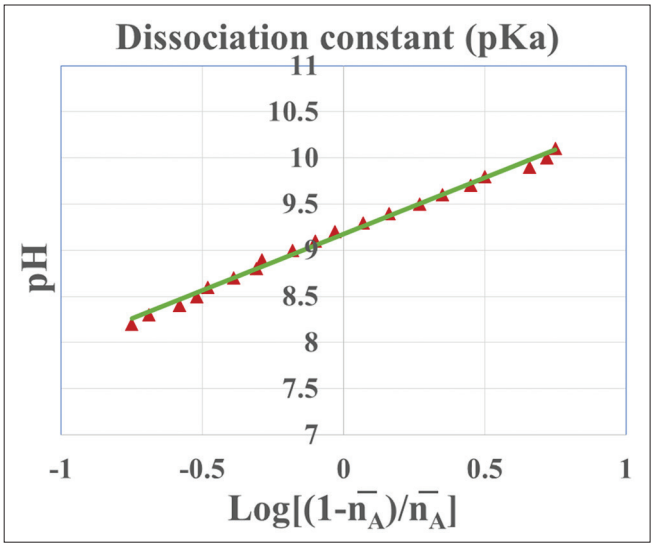

Figure 3: Linear plot for calculation of dissociation constant of ligand (**HL**).

3.4. Spectral and Analytical Studies of HL

3.4.1. IR spectrum

In the IR spectrum (Figure S1) of **HL,** observed peaks at 3333 cm^{-1} and at 3190 cm^{-1} are due to NH asymmetric and symmetric stretching. The peaks observed at 3072–2843 cm^{-1} are due to υ (C-H). The sharp bands at 1677 and 1572 cm^{-1} are attributable to amide υ (C=O) and azomethine υ (C=N) stretching modes, respectively. The peaks at 1514 & 1487 cm^{-1} are due to aromatic υ (C=N & C=C) stretching frequencies, and the sharp bands at 1340 and 1239 cm^{-1} are attributable to υ (C-N) and υ (C-O) vibrational modes, respectively.

3.4.2. ^{1}H-NMR spectrum

The spectrum (Figure S6) of **HL** was recorded in DMSO-d_6 at 400 MHz instrumental frequency. The signal at δ 12.23 ppm (s, 1H) can be attributed to the NH group. The proton of azomethine (s, N=CH) is recorded at 8.46 ppm and other signals observed are; δ 8.31 ppm (d, 2H, Py-H), δ 8.24 ppm (d, 2H, Ph-H), δ 7.94 ppm (d, 2H, Ph-H) and δ 7.85 ppm (d, 2H, Py-H).

3.4.3. ^{13}C-NMR spectrum

The ^{13}C-NMR spectrum (Figure S7) of **HL** was recorded at 100 MHz instrumental frequency in DMSO-d_6 solvent. The ^{13}C chemical shifts displayed at δ 160.95 ppm and δ 149.49 ppm correspond to C=O and CH=N groups, respectively. The peaks appeared at chemical shift values δ 139.10 ppm, 128.21 ppm, and 125.03 ppm correspond to aromatic pyridine carbons. The peaks at δ 159.44 ppm, 131.10 ppm, 110.46, 107.80 ppm, and 102.59 ppm are due to chemical shifts of NO_2-substituted aromatic phenyl carbons.

3.5. Mass and Elemental Analyses

The mass spectrum (Figure S8) of **HL** exhibited a dominant base peak at m/z 287.0781 attributable to molecular ion $[M+1]^+$ peak. Elemental analyses, Found %: C, 54.49; H, 3.55; N,19.60; Calcd %: C, 54.55; H, 3.52; N, 19.57; indicated composition of the compound as $C_{13}H_{10}N_4O_4$.

3.6. UV-Visible Spectrum

The UV-visible spectrum (Figure S13) of **HL** in DMSO (10^{-3} M) was recorded at the wavelength range of 200–800 nm. The spectrum displayed bands at 255 nm (39,215.69 cm^{-1}) and 346 nm (28,901.73 cm^{-1}) for π→π* and n→π* transitions due to the presence of aromatic groups and other chromophores.

3.7. Spectral Studies of Metal Complexes

3.7.1. FT-IR spectral studies

IR spectra and the respective data of all systems under consideration of the present investigation presented in Figure (S1-S5) & Table S1,

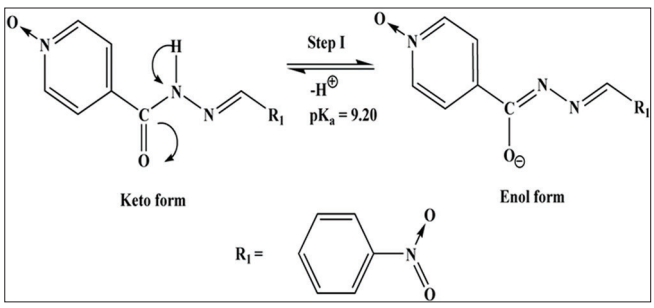

Figure 4: Keto-enol tautomerism of ligand (**HL**).

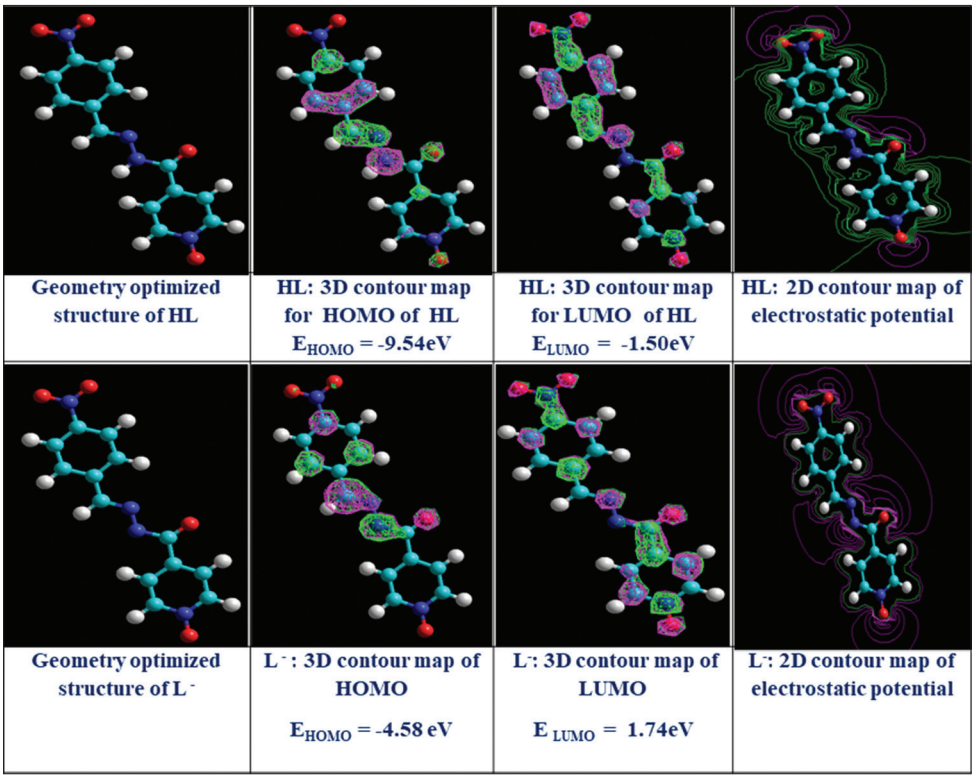

Figure 5: HyperChem 7.5 Computed Molecular Oritals of **HL** and its ionized form (**L^-**).

provide useful information of coordination sites in the ligand that involved in bonding. The metal complexes showed a new broad band in the area of 3410–3444 cm^{-1} indicating H_2O molecules in coordinated form. The observed bands of υ (NH) at 3333 cm^{-1} and 3190 cm^{-1} in ligand which are not noticeable in all IR spectra of metal complexes suggest coordination of the ligand with respective metal ion through dissociation of NH proton through its enol form. The enolization at the CONH group followed by dissociation of the enol proton is understandable by the disappearance of υ (C=O) and υ (N-H) bands in the IR spectra of the complexes. Further, it is supported by the appearance of new bands at 1217–1348 cm^{-1} and 1504–1597 cm^{-1} which corresponds to enolate υ (C-O) and iminol υ (C=N), respectively, inferring metal to ligand bond formation through enolate oxygen [35]. The shift of band at 1572 cm^{-1} of azomethine group υ (C=N) to lower frequency indicates the donation of a lone pair of electrons from bonding molecular orbital type localized on the nitrogen of azomethine in all metal complexes. The metal complexes showed new bands in the far IR region at 419–582 cm^{-1} and 353–407 cm^{-1} due to vibrations in metal-to-ligand coordinated bonds M-O and M-N, respectively. The IR spectral results thus augment the bidentate nature of the candidate ligand.

3.8. Electronic Spectra and Magnetic Properties

The electron absorption spectra of ligand and its complexes were recorded in DMSO (10^{-3} M) solution within the wavelength of 200–800 nm, and the spectra depicted in Figure (S13-S17). The new absorption bands at the wavelength region of 257–331 nm (38,910.51 cm^{-1}–30,211.48 cm^{-1}) in all systems recorded are ascribable to π→π* and n→π* transitions associated with bound ligand. The absorptions displayed at region 410–730 nm (25,974.03 cm^{-1}–13,698.63 cm^{-1}) are mainly due to *d* →*d* transitions in all metal complexes [36]. The spectrum of maroon-colored **cobalt** complex exhibited broad bands at 500 nm (20,000.00 cm^{-1}) and 730 nm (13,698.63 cm^{-1}) due to spin-allowed *d*→*d* transitions, and the calculated magnetic moment value is 4.38 B.M. The spectrum of orange-colored **nickel** complex displayed absorptions at 410 nm (24,390.24 cm^{-1}), 593 nm (16,863.41 cm^{-1}), and 699 nm (14,306 cm^{-1}), which are assignable to *d*→*d* transitions. Its measured value of the magnetic moment is 2.82 B.M. The dark green colored **copper** complex displayed spectral bands at 385 nm and 473 nm (25,974.03 cm^{-1} and 21,141.65 cm^{-1}) assignable to CT and *d*→*d* transitions. The deduced magnetic moment value of 1.73 B.M for the **copper** complex is in accordance of the predicted value. The absorption spectrum of orange yellow colored diamagnetic **zinc** complex indicated a band at 409 nm (24,449.88 cm^{-1}) ascribable to CT transition only. Above mentioned spectral and magnetic properties of complexes notify octahedral geometry.

3.9. Thermal Analysis

Thermal degradation of the metal complexes was examined using TGA and DTA methods up to the maximum temperature of 1000°C and representative plots are posted in Figure 6. The thermogram of the **Co(II) complex** recorded a weight loss of 84.71% after total thermal loss of coordinated moiety. A minimum weight loss (5.99%) up to 225°C is indicative of the loss of bound water molecules in the complex [37]. Subsequently sudden decrease in weight of 45.46% at 286 – 430°C range contributable to the partial decomposition of ligand moiety is also evidenced an exothermic peak on the DTA curve at 345°C indicating it as an exothermic process. At 430 – 699°C, the further gradual weight loss of 33.26% is also an exothermal process, which is substantiated through the appearance of an exothermic peak at 652°C in DTA curve. The final residual mass after exothermic loss of surrounding coordinated ligand moiety is assignable to the formation of the stable oxide of cobalt.

The thermogram of the **Ni(II) complex** recorded a total weight degradation of 88.52%. The complex displayed a weight loss (5.95%) around 170 – 228°C representing a loss of coordinated water molecules. A steady decrease in weight of 82.57% at the temperature region of 367 – 598°C through the release of heat as evident from an exothermic peak at 462°C in the DTA curve infers complete decomposition of organic

moiety. The remaining mass at the end region of the thermogram is suggestive of formation for metal oxide.

The thermogram of the **Cu(II) complex** showed a total weight loss of 87.44% after decomposition of the surrounding moiety. The initial weight loss (5.44%) up to 300°C corresponds to the thermal evaporation of coordinated water molecules. Subsequent weight loss (63.54%) around 300 – 399°C is indicative of the partial decomposition of ligand moiety with the release of heat as indicated by an exothermic peak recorded in the DTA curve at 345°C. Further gradual loss in weight observed in the range 399°C–670°C, ascribable to the total degradation of (18.46%) ligand moiety is also apparently an exothermic process as evident from the DTA curve, which showed a peak at 625°C. The final residue left at the end is ascribable to stable metal oxide [38].

The thermal decomposition of the **Zn(II) complex** showed a total weight loss of 86.32%. The initial weight loss of 5.35% up to 300°C matches to the loss of coordinated water molecules. The succeeding weight loss of 52.56% around 300 – 433°C due to the fractional decomposition of ligand moiety is an exothermic process and is augmented thorough recorded exothermic peak on the DTA curve at 355°C. Further gradual decomposition in the temperature region 433°C–699°C which is also an exothermic process as indicated on the DTA curve at 642°C notifies loss of 28.41% remaining organic moiety. The leftover residue at the completion of degradation of surrounded bound moiety in the complex is indicative of metallic oxide formation.

3.10. SEM and EDX Analysis

The surface morphology images of ligands and complexes were obtained by scanning electron microscopy technique, and are presented in Figure 7. The surface morphology signified a poly hexagon-like appearance for ligand (**HL**), cubes arrangement for **Co(II)** complex,

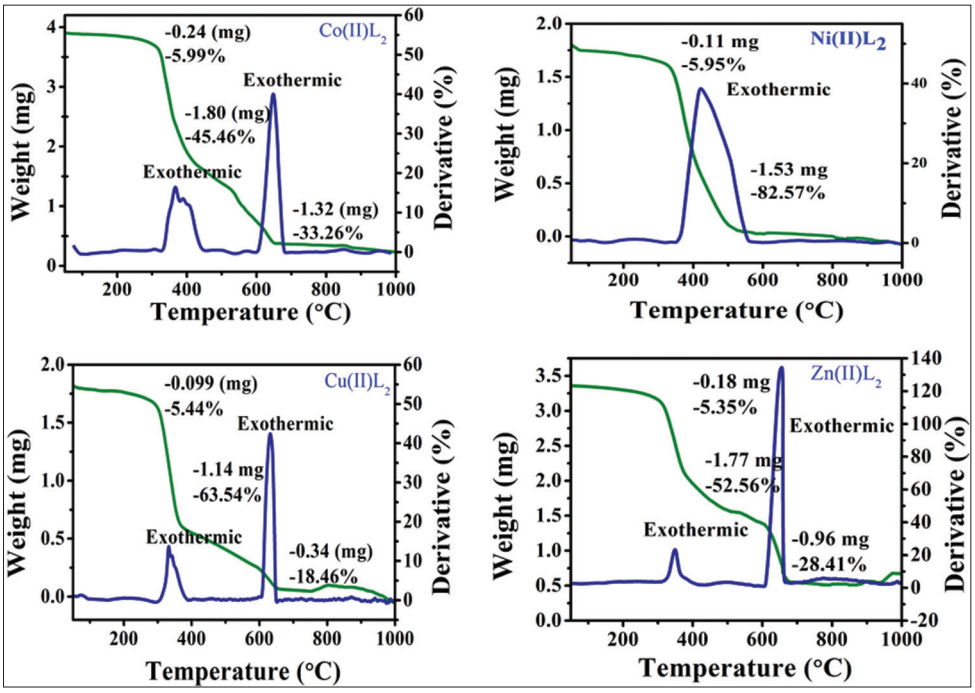

Figure 6: TGA and DTA curves of metal complexes.

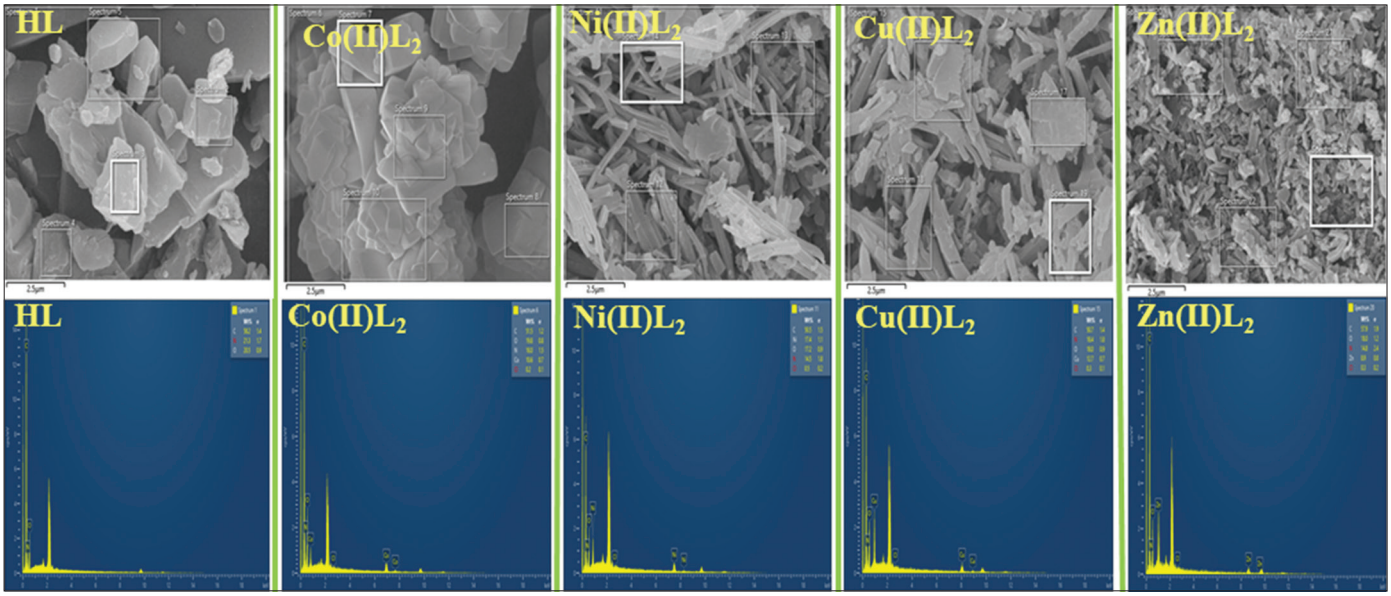

Figure 7: SEM images and EDX plots.

nanorods-like texture for **Ni(II)** complex, sticks-like appearance for **Cu(II)** complex, and polyhedral blocks texture for **Zn(II)** complex indicating morphologies distinctive of each compound. The EDX analysis helped in assessing qualitative elemental composition in all the examined systems [39]. The information derived from the EDX analysis of all systems is approximately in congruence with the elemental composition evidenced through the mass and thermal analyses.

3.11. ESR Studies

The electron spin resonance spectrum of the copper complex recorded at room temperature in DMSO solution is presented in Figure 8. The g-tensors observed in order; $g_{\parallel}$ (2.12952) > $g_{\perp}$ (2.05883) provided useful information ascertaining slight distortion in geometry as axial symmetry with unpaired electron in a dx^2-y^2 orbital. The Hathway expression was used to calculate the exchange interaction coupling constant (G) value of **Cu(II)L_2**, where $G = (g_{\parallel}-2)/(g_{\perp}-2)$ [40]. By considering EPR spectral parameters in the above copper complex, the calculated G value of 2.202, which is lower than 4 signify an exchange interaction between the metal ion and ligand at room temperature.

Based on the above results of various spectral and analytical data acquired for ligands and complexes, and also taking an account of the outcome of equilibrium studies and computed molecular properties discussed earlier into consideration the octahedral geometrical structures are depicted for all complexes as shown in Figure 1.

3.12. DNA Binding Studies

3.12.1. Absorption studies

The absorption titrations were conducted to study the interaction of all the complexes and ligands with CT-DNA in the Tris-HCl buffer medium. The absorption spectra in all systems under investigation were examined in the absence and presence of CT-DNA. The titrations were conducted at the constant concentration of title compounds and varying CT-DNA concentrations. The corresponding absorption spectra were obtained after step-wise fractional addition of CT-DNA solution as shown in Figure 9. These spectra denoted a reduction in the intensity of peaks (hypochromism) and redshift (bathchromism), which may be probably due to hydrophobic π→π* stacking type of interface links between purine and pyrimidine base pairs of DNA and aromatic rings of the coordinated ligand in metal complexes of the present investigation.

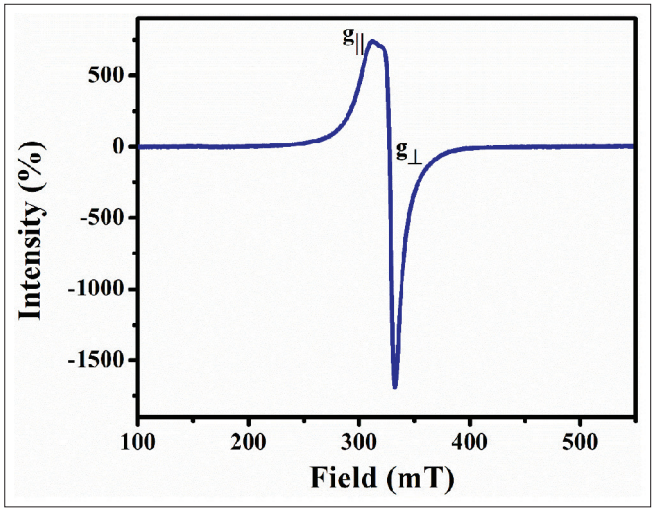

Figure 8: Electron spin resonance spectrum of **Cu(II)** complex in DMSO solvent at room temperature.

Subsequently from the recorded absorption data, the affinity strength of complexes is evaluated by deducing the binding constant K_b by adopting a known equation [29, 41]. The calculated K_b values for all the systems under investigation are posted in Table 1. These results obtained for all the systems of the present investigation, indicate higher binding strength of copper complex**.**

2.13. Fluorescence Studies

To further confirm the binding of ligand and metal complexes with CT-DNA, employing an ethidium bromide (EB) fluorescent probe, a competitive binding emission experiment was conducted. The decrease in fluorescence intensity of EB bound to DNA is measured to deduce the binding strength of title compounds with DNA. On addition of ligand and metal complexes to CT-DNA already treated with EB in respective titrations, a considerable reduction in the emission intensity (Figure 10) was noted, ascertaining the competitive binding of compounds, and thus influencing the equilibrium reaction of [DNA-EB] adduct formation [30, 42]. The calculated K_{sv} and K_b values indicated more affinity of copper complex (Table 1).

3.14. Antioxidant Studies

The scavenging method of DPPH free radical is adopted for all systems under investigation to assess their antioxidant properties by measuring absorbance values at 517 nm [43], and the results are posted in Figure 11.

The measured free radical scavenging activity is noted as 62.17% for ascorbic acid, 54.95% for **Co(II)** complex, 49.18% for **Ni(II)** complex, 53.99% for **Cu(II)** complex, 46.49% for **Zn(II)** complex, and 41.55% for **HL**, at the concentration of compounds of 0.2 to 1.0 (mg/mL). The activity noted for ligand is moderate, and metal complexes displayed considerable activity, while the reference compound revealed 62.17% higher activity. The observed antioxidant activity is high in cobalt and copper complexes. Such an experimental observation infers the role of metal ions in bound form with ligand in effecting the antioxidant properties.

3.15. Antibacterial Activity

The antibacterial activity assay was executed by spread plate method. The samples were dissolved in 1mL of DMSO. All test compounds of the present investigation were analyzed for their minimum inhibitory concentrations (MIC) against chosen bacteria [44] by taking 25 µL, 50 µL, and 75 µL of sample solution and making up to 100 µL volume, and also 100 µL sample solution as such without further dilution [45]. These solutions were tested against *Staphylococcus* and *Bacillus* as Gram-positive bacteria, as well as *E. coli* and *Klebsiella* Gram-negative bacteria. The above sample solutions, 100 µL each were loaded into the wells and incubated at 37°C for 18–24 h in a bacterial incubator.

After the incubation period, the bacterial plates appeared as shown in Figure 12. The results indicate the antibacterial activity of **Co(II)L_2**, **Ni(II)L_2**, and **Zn(II)L_2** against Gram-positive and Gram-negative bacterial pathogens, while **HL** and **Cu(II)L_2** have not shown any activity. The obtained MIC values are tabulated in Table 2 & Tables S2-S5.

2.16. Antifungal Activity

The minimum inhibitory concentrations (MIC) for antifungal action of title compounds were assayed by taking 100 µL of the sample as such without dilution and other sets as 25 µL, 50 µL, and 75 µL of sample, each one diluted to a final volume of 100 µL with solvent. The antifungal effect was assayed against *Candida* and *Aspergillus* by loading the plate wells with above each 100 µL volume of sample

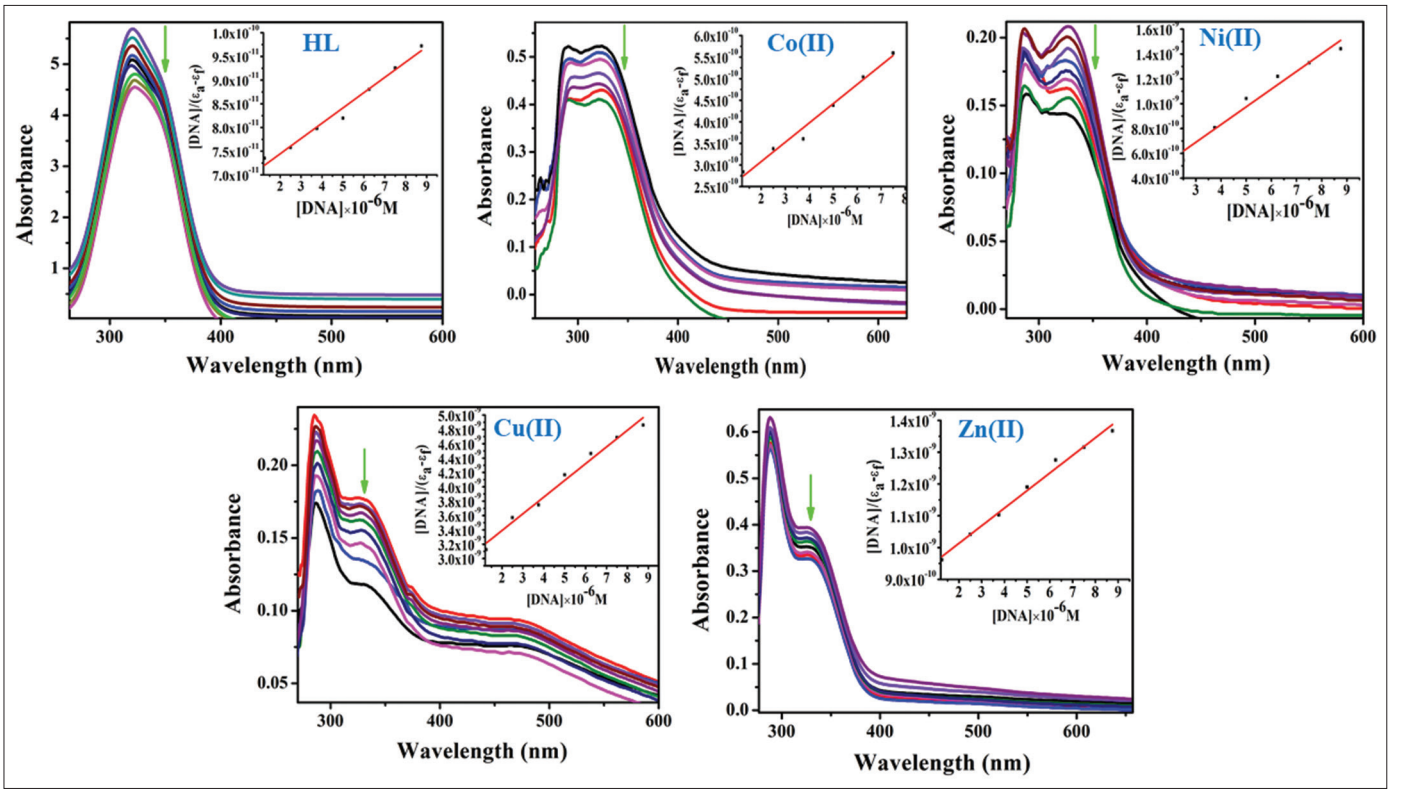

Figure 9: Absorption spectra of studied compounds upon gradual addition of CT-DNA, insert: the respective linear plots [DNA]/($|\varepsilon_a-\varepsilon_f|$) vs [DNA].

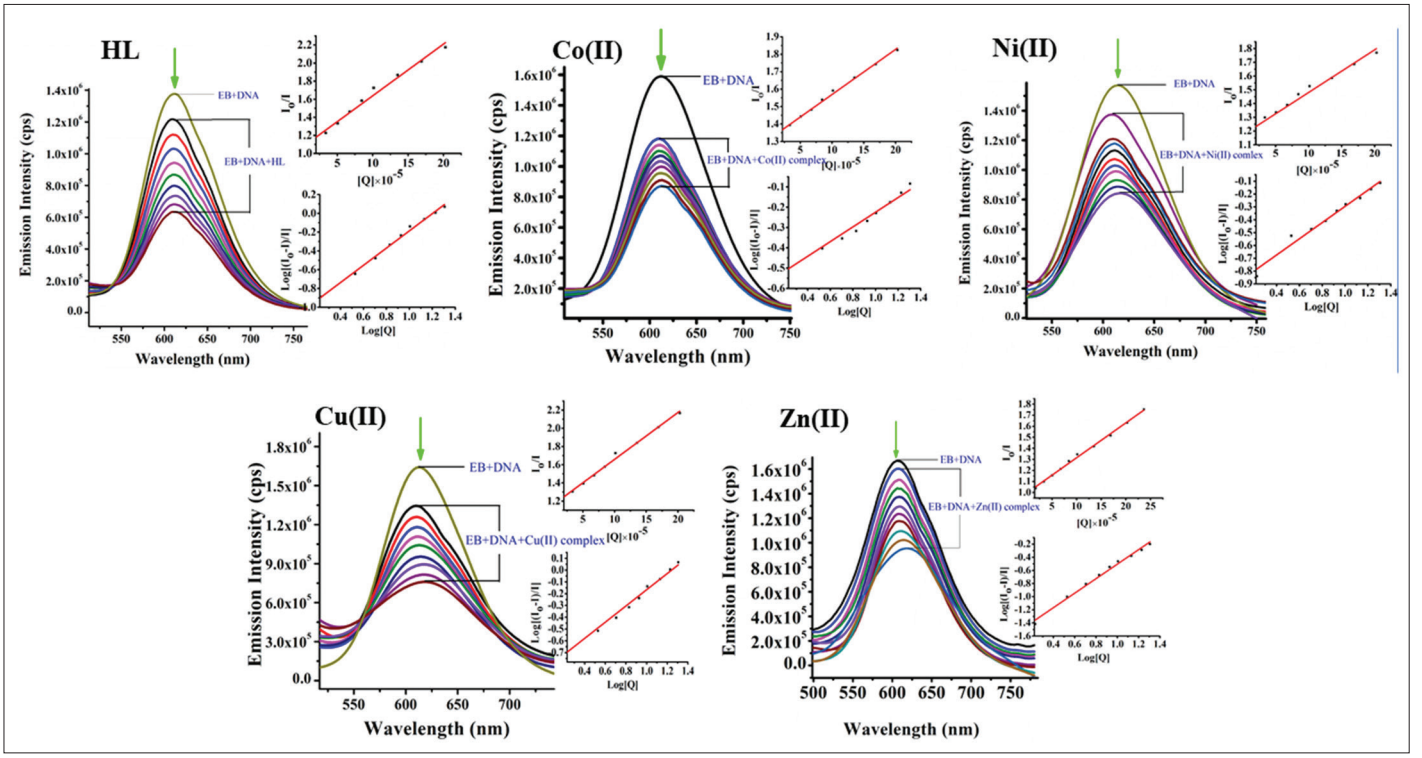

Figure 10: Emission spectra of title compounds recorded at wavelength 610 nm (λex =520 nm).

solutions of varying concentration and incubating at 25°C for 96 h [46].

The fungal plates were observed after incubation time as shown in Figure 13. The results indicate the antifungal activity of ligand and complexes against both pathogens and no activity for **Cu(II)L_2** complex and **HL**. The respective measured MIC values for compounds are given in Table 3 & Tables S6 and S7.

2.17. Cytotoxicity

MCF-7 (breast adenocarcinoma) cancer cell lines were used in the *in vitro* MTT assay method to quantity the cytotoxicity of the synthesized title compounds. The experimental results have shown concentration-dependent activity, as indicated in Figure 14, wherein an increase in the concentration of test samples (5 µg, 10 µg, 25 µg, 50 µg, and 100 µg) resulted decrease of cell viability, indicating an increased cytotoxicity [47]. Morphological changes evidential in microscopic pictures after treatment cells with compounds are given in Figure 15. The IC_{50} values of compounds are presented in Table 4 & Tables S8-S12. Among all synthesized title compounds **Cu(II)** complex showed more potential anticancer activity.

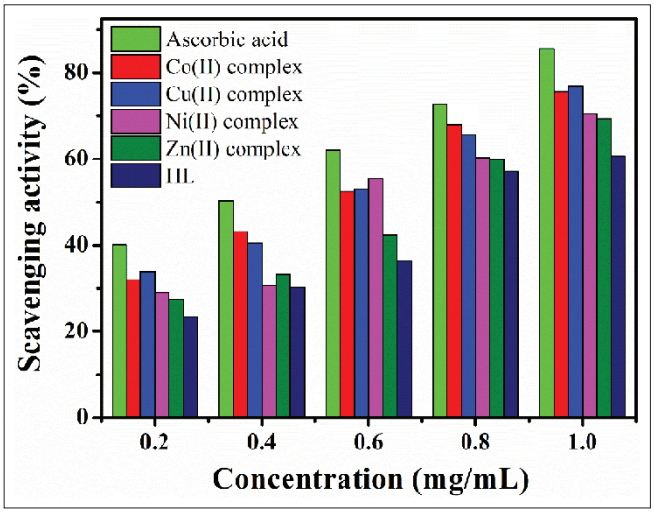

Figure 11: Bar plot showing free radical scavenging percentage.

Table 1: Data showing Kb and Ksv values of **HL** and its metal complexes

	Absorption Method	Fluorescence Method		
Compounds	K_b	K_b	K_{sv}	R
HL	4.78×10^4 M^{-1}	3.46×10^4 M^{-1}	4.28×10^4 M^{-1}	0.99
Co (II) L_2	4.04×10^5 M^{-1}	1.34×10^5 M^{-1}	1.38×10^5 M^{-1}	0.98
Ni (II) L_2	3.46×10^5 M^{-1}	1.14×10^5 M^{-1}	9.83×10^4 M^{-1}	0.99
Cu (II) L_2	4.97×10^5 M^{-1}	1.47×10^5 M^{-1}	1.43×10^5 M^{-1}	0.97
Zn (II) L_2	6.13×10^4 M^{-1}	9.73×10^4 M^{-1}	8.69×10^4 M^{-1}	0.99

Table 2: Zone of inhibition (mm) for loaded samples of 100 µL against bacterial pathogens

S.No	Sample Name	Gram Positive Bacterial pathogens		Gram Negative Bacterial pathogens	
		Staphylococcus	*Bacillus*	*E. coli*	*Klebsiella*
1	Co (II) L_2	10 mm	12 mm	10 mm	14 mm
2	Ni (II) L_2	11 mm	12 mm	10 mm	13 mm
3	Cu (II) L_2	-	-	-	-
4	Zn (II) L_2	10 mm	10 mm	10 mm	12 mm
5	HL	-	-	-	-
6	Standards	14 mm	14 mm	14 mm	12 mm

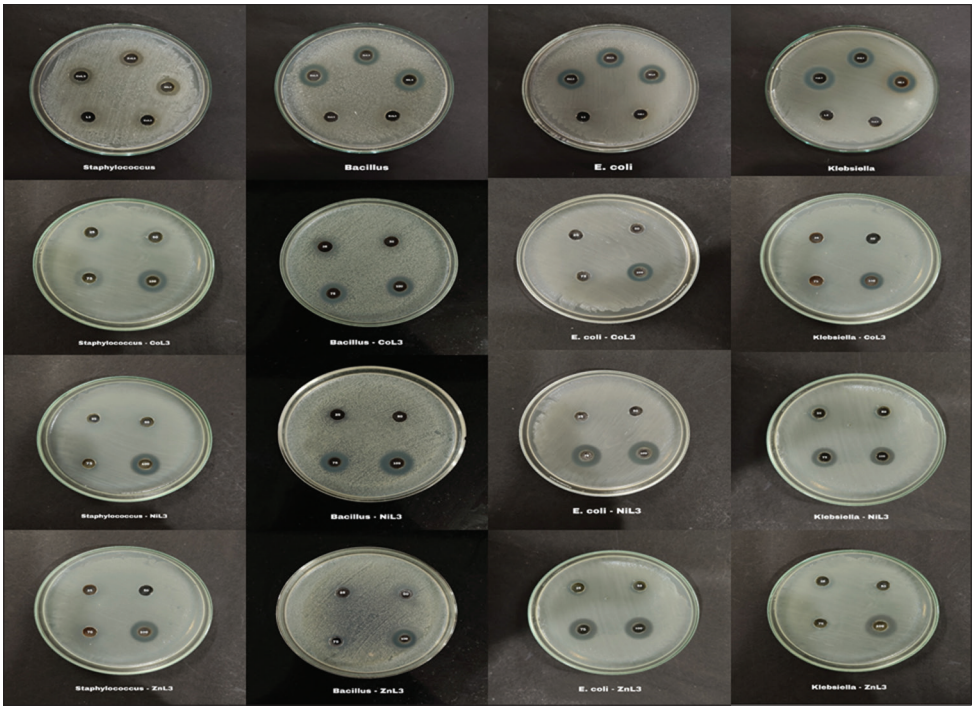

Figure 12: Bacterial plates indicating zone of inhibition.

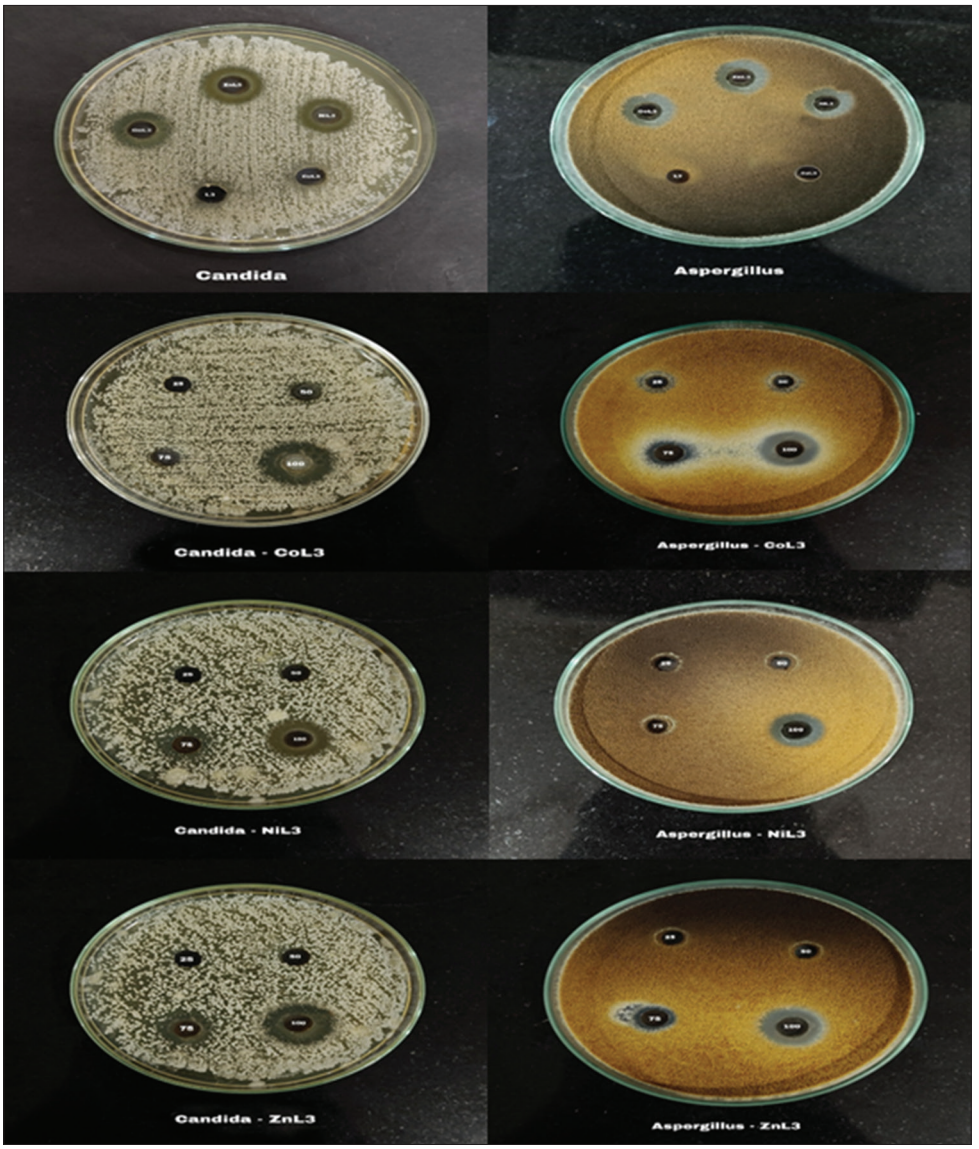

Figure 13: The plates showing zone of inhibition for fungal pathogens.

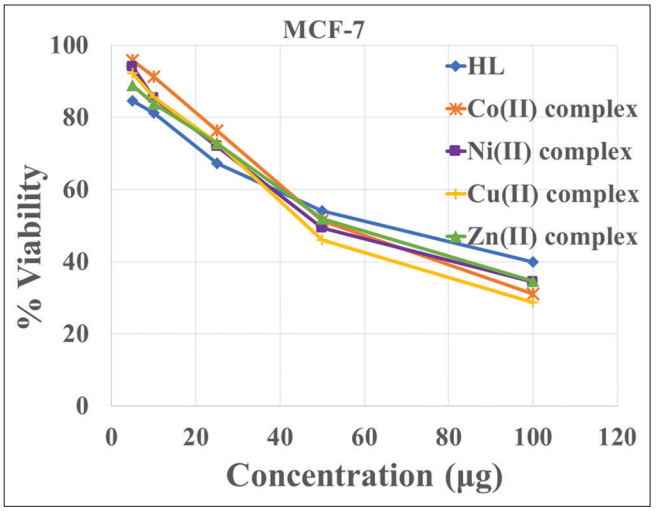

Figure 14: Effect on the cell viability of MCF-7 cell lines on increasing the concentration of ligands and complexes.

Table 3: Fungal pathogens study on *Candida* and *Aspergillus*

S.No	Sample Name	Fungal pathogens	
		Candida	***Aspergillus***
1	Co (II) L_2	10 mm	10 mm
2	Ni (II) L_2	10 mm	10 mm
3	Cu (II) L_2	-	-
4	Zn (II) L_2	12 mm	12 mm
5	HL	-	-
6	Standards	14 mm	14 mm

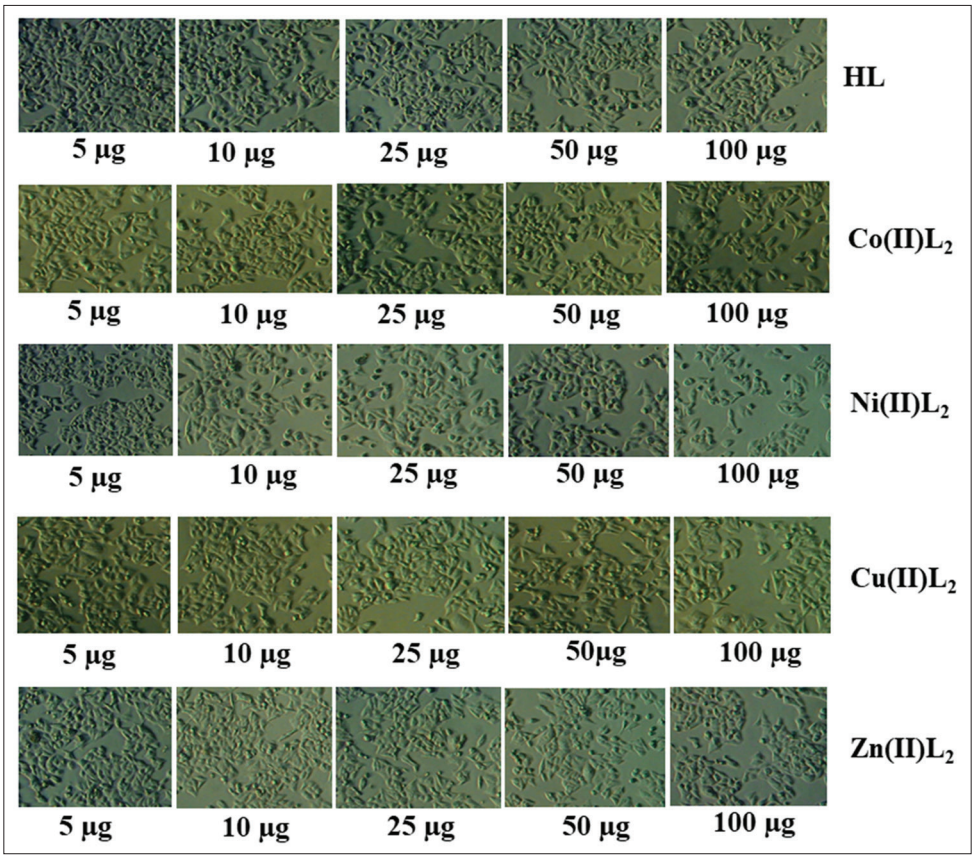

Figure 15: Morphological changes in MCF-7 cell lines, treated with varying concentrations of ligands and complexes**.**

Table 4: The IC_{50} values (µg/mL) for **HL** and its complexes treated with MCF-7 cell lines

S.No	Sample Name	IC50 (µg/mL)
		MCF-7
1	HL	71.09
2	Co (II) L_2	65.75
3	Ni (II) L_2	65.67
4	Cu (II) L_2	60.49
5	Zn (II) L_2	66.65
6	Cisplatin (µM)	5.74

4. CONCLUSION

The title compound 4-(2-(4-nitrobenzylidene)hydrazinecarbonyl) pyridine1-oxide (**HL**) and its cobalt, nickel, copper, and zinc metal complexes were synthesized and characterized. Equilibrium studies of the ligand (**HL**) in 40% DMF-H_2O medium inferred the monoprotic nature of the ligand with its pKa value as 9.20. HyperChem computational studies are informative in understanding the chelation properties of title hydrazone and its modes of bonding with metal ions. The analytical and spectral data inferred the formation of 1:2 [ML] metal complexes. SEM images recorded distinct surface texture in each of the title compounds. Thermographs of metal complexes indicated two-step decompositions of bound ligand in all accompanied by a release of energy as evidenced from respective DTA curves. The ESR spectral information of the copper complex is assertive in understanding an anisotropic distribution of electron density around the central metal atom. In CT-DNA binding studies of **HL**, **Co(II)L_2**, **Ni(II)L_2**, **Cu(II)L_2**, and **Zn(II)L_2** complexes, the K_b values which define their binding affinity obtained through absorption method (**Cu(II)L_2**, **Co(II)L_2**, **Ni(II)L_2** and **Zn(II)L_2** >**HL**:4.97×10^5 M^{-1}> 4.04×10^5 M^{-1}> 3.46×10^5 M^{-1}> 6.13×10^4 M^{-1}> 4.78×10^4 M^{-1}), are in same order of K_b values calculated from fluorescence method (**Cu(II) L_2**, **Co(II)L_2**, **Ni(II)L_2**, and **Zn(II)L_2** >**HL**: 1.47×10^5 M^{-1}> 1.34×10^5 M^{-1}> 1.14×10^5 M^{-1}> 9.73×10^4 M^{-1}> 3.46×10^4 M^{-1}). Radical scavenging activity studies inferred substantial activity of complexes, and ligands showed moderate activity. The percentage of radical scavenging activity of 54.95% in **Co(II)L_2** is closer to the activity of reference recorded as 62.17%. Antibacterial and antifungal studies inferred potential activity for **Co(II)L_2**, **Ni(II)L_2**, and **Zn(II)L_2** only. The experimental observations of *in vitro* cytotoxicity screening of synthesized compounds revealed that metal complexes are more potent than ligands**.** The order for anticancer activity of complexes is **Cu(II) L_2** > **Ni(II)L_2** > **Co(II)L_2** > **Zn(II)L_2** > **HL**.

5. ACKNOWLEDGMENTS

Authors N. Anitha and Dr. Ch. Sarala Devi acknowledge CSIR-UGC (Council of Scientific and Industrial Research-University Grants Commission), New Delhi, India, for solid financial support as UGC-JRF (Junior Research Fellowship) to Nayakini Anitha, file no: F.16-6 (DEC.2016)/2017 (NET) and also extend gratitude to the Head Department of Chemistry, Osmania University, Hyderabad, Telangana, for the research facility. Authors are thankful to Dr. Mudavath Ravi, for providing instrumental facilities.

6. REFERENCES

1. Z. Shu-Feng, Z. Wei-Zhu, (2017) Drug design and discovery: Principles and applications, ***Molecules***, **22(2)**: 279.

2. S. Sandeep, V. Divya, (2018) ***Chapter 2-Drug Discovery and Development: An Overview. Pharmaceutical Medicine and Translational Clinical Research***, United States: Academic Press, p19-32.
3. R. Liu, J. Cui, T. Ding, Y. Liu, L. Hong, (2022) Research progress on the biological activities of metal complexes bearing polycyclic aromatic hydrazones, ***Molecules***, **27:** 8393.
4. A. C. Ekennia, E. C. Ibezim, O. C. Okpareke, C. U. Ibeji, C. J. O. Anarado, I. Babahan, B. Coban, B. Abulhasanov, F. Cömert, O. T. Ujam, (2019) Novel 3-Hydroxy-2-naphthoic hydrazone and Ni(II), Co(II) and Cu(II) complexes: Synthesis, spectroscopic characterization, antimicrobial, DNA cleavage and computational studies, ***Applied Organometallic Chemistry***, **33:** e4913.
5. A. Saeed, M. I. Arshad, B. Michael, A. C. Fantoni, Z. Y. D. Espinoza, M. F. Erben, (2016) On the roles of close shell interactions in the structure of acyl-substituted hydrazones: An experimental and theoretical approach, ***Spectrochimica Acta Part A: Molecular and Biomolecular Spectros***copy, **157:** 138-145.
6. H. Kargar, F. M. Mehdi, K. S. Munawar, (2024) Metal complexes incorporating tridentate ONO pyridyl hydrazone Schiff base ligands: Crystal structure, characterization and applications, ***Coordination Chemistry Reviews,*** **501:** 215587.
7. W. Jenna, M. Sarah, (2019) The use of hydrazones for biomedical applications, ***SLAS Technology***, **24(2)**: 161-168.
8. C. M. Mustapha, C. P. Udaysinha, V. S. Supriya, R. D. Uttam, S. Y. Ramesh, (2017) A review on quinoline hydrazone derivatives as a new class of potent antitubercular and anticancer agents, ***BJBAS***, **6(4):** 354-361.
9. T. M. Sun, W. Yu-Cai, F. Wang, J. Z. Du, C. Q. Mao, C. Y. Sun, R. Z. Tang, Y. Liu, J. Zhu, Y. H. Zhu, X. Z. Yang, J. Wang, (2014) Cancer stem cell therapy using doxorubicin conjugated to gold nanoparticles via hydrazone bonds, ***Biomaterials***, **35(2)**: 836-845.
10. S. A. Khan, M. J. Akhtar, (2022) Structural modification and strategies for the enhanced doxorubicin drug delivery, ***Bioorganic Chemistry,*** **120:** 105599.
11. J. Wahbeh, M. Sarah, (2019) The use of hydrazones for biomedical applications. ***SLAS TECHNOLOGY: Translating Life Sciences Innovation***, **24(2):** 161-168.
12. S. L. Scinto, D. A. Bilodeau, R. Hincapie, W. Lee, S. S. Nguyen, M. Xu, Q. W. Am Ende, M. G. Finn, K. Lang, Q. Lin, J. P. Pezacki, J. A. Prescher, M. S. Robillard, J. M. Fox, (2021) Bioorthogonal chemistry, ***Nature Reviews Methods,*** **1:** 30.
13. O. J. B. de Carneiro, T. C. C. França, S. R. LaPlante, J. D. F. Villar, (2020) Synthesis and biological activity of hydrazones and derivatives: A review. ***Mini-Reviews in Medicinal Chemistry***, **20(27)**: 342-368.
14. P. Kumar, A. Rai, M. Singh, D. Kumar, A. K. Sahdev, V. Raj, (2016) Review on the pharmacological activities of hydrazones derivatives. ***EC Pharmaceutical Science***, **2(3)**: 278-306.
15. M. Asif, A. Husain, (2013) Analgesic, anti-inflammatory, and antiplatelet profile of hydrazones containing synthetic molecules. ***Journal of Applied Chemistry***, **1-7:** 247203.
16. M. A. Shah, A. Uddin, M. R. Shah, I. Ali, R. Ullah, P.A. Hannan, H. Hussain, (2022) Synthesis and characterization of novel hydrazone derivatives of isonicotinic hydrazide and their evaluation for antibacterial and cytotoxic potential. ***Molecules***, **27(19)**: 6770.
17. L. Popiołek, A. Biernasiuk, A. Berecka, A. Gumieniczek, A. Malm, M. Wujec, (2018) New hydrazide-hydrazones of isonicotinic acid: Synthesis, lipophilicity and *in vitro* antimicrobial screening, ***Chemical Biology and Drug Design***, **91(4)**: 915-923.
18. D. R. Richardson, P. Ponka, (1998) Pyridoxal isonicotinoyl hydrazone and its analogs: Potential orally effective iron-chelating agents for the treatment of iron overload disease, ***Journal of Laboratory and Clinical Medicine***, **131(4):** 306-315.
19. Z. Shahab, A. Yasamin, N. Maryam, S. Mojgan, (2020) The effects study of isoniazid conjugated multi-wall carbon nanotubes nanofluid on *Mycobacterium tuberculosis*, ***International Journal of Nanomedicine,*** **15:** 5901-5909.
20. A. Suman, N. Priyatosh, D. Alakesh, D. Abhijit, B. Nabajyoti, K. D. Asim, P. Surajit, (2024) A review on metal complexes and its anti-cancer activities: Recent updates from in vivo studies, ***Biomedicine and Pharmacotherapy***, **171:** 116211.
21. M. C. Heffern, N. Yamamoto, R. J. Holbrook, A. L. Eckermann, T. J. Meade, (2013) Cobalt derivatives as promising therapeutic agents, ***Current Opinion in Chemical Biology,*** **17(2)**: 189-196.
22. J. A. Schwartz, E. K. Lium, S. J. Silverstein, (2001) Herpes simplex virus type 1 entry is inhibited by the cobalt chelate complex CTC-96, ***Journal of Virology***, **75(9)**: 4117-4128.
23. J. E. Weder, C. T. Dillon, T. W. Hambley, B. J. Kennedy, P. A. Lay, (2002) Copper complexes of non-steroidal anti-inflammatory drugs: An opportunity yet to be realized, ***Coordination Chemistry Reviews***, **232(1-2):** 95-126.
24. K. Ni, M. Nicolás, K. Johannes, (2024) Highly cytotoxic Cu(II) terpyridine complexes as chemotherapeutic agents, ***Dalton Transactions***, **53:** 8223-8228.
25. F. Tisato, C. Marzano, M. Porchia, M. Pellei, C. Santini, (2010) Copper in diseases and treatments, and copper-based anticancer strategies, ***Medicinal Research Reviews***, **30(4)**: 708-749.
26. M. Pellei, F. Del Bello, M. Porchia, C. Santini, (2021) Zinc coordination complexes as anticancer agents, ***Coordination Chemistry Reviews***, **445:** 214088.
27. P. P. Choudhari, P.R. Yawale, S. S. Ubarhande, M. P. Wadekar, (2020) Study of stability constant of complexes of the metal ions Fe(III), Mn(II), Cr(III) and Ti(III) with substituted 2-oxo-2H-chromene-3-carbohydrazide derivatives in 70% DMF-Water solvent at 32^0 C, ***JETIR***, **7(2)**: 2349-5162.
28. N. Anitha, P. J. Laxmi, M. Ravi, C. Sarala Devia, (2023) Experimental and theoretical studies on structural aspects of transition metal complexes of isonicotinoyl N-oxide hydrazone: Their DNA-binding interaction and cytotoxicity, ***Applied Organometallic Chemistry***, **37:** e7289.
29. M. Ravi, B. Ushaiah, C. Kishan Prasad, K. Sudeepa, P. Ravindar, S. N. T. Sunitha, C. Sarala Devi, (2019) Molecular docking, QSAR properties and DNA/BSA binding, anti-proliferative studies of 6-methoxybenzothiozole imine base and its metal complexes, ***Journal of Biomolecular Structure and Dynamics***, **38(10)**: 1538-0254.
30. C. Kishan Prasad, M. Ravi, B. Aparna, K. Sudeepa, P. Ravinder, C. Sarala Devi, (2022) Spectroanalytical, computational, DNA/BSA binding and in vitro cytotoxic activity studies of new transition metal complexes of novel aryl hydrazone, ***Journal of Molecular Structure***, **1252:** 132126.
31. a) C. Kishan Prasad, M. Ravi, B. Ushaiah, V. Srinu, R. K. Eslavath, C. Sarala Devi, (2016) Synthesis, characterization, DNA interactions, DNA cleavage, radical scavenging activity, antibacterial, anti-proliferative and docking studies of new transition metal complexes, ***Journal of Fluorescence***, **26(1):** 189-205. b) K. Sudeepa, N. Narsimha, B. Aparna, S. Sreekanth, A. V. Aparna, M. Ravi, M. Jaheer, C. Sarala Devi, (2018) Synthesis, spectral characterization, antimicrobial, DNA interactions and molecular modeling studies of metal complexes of 1, 3-benzothiazole carbohydrazone, ***Journal of Chemical***

Sciences, **130(52)**: 1-13.

32. J. E. Philip, S. A. Antony, J. E. Sneha, M. R. K. Prathapachandra, M. P. Velayudhan, (2018) Design, synthesis, antimicrobial and antioxidant activity of 3-formyl chromone hydrazone and their metal (II) complexes, *Inorganica Chimica Acta*, 469: 87-97.
33. T. Arora, J. Devi, A. Boora, B. Taxak, S. Rani S, (2023) Synthesis and characterization of hydrazones and their transition metal complexes: Antimicrobial, antituberculosis and antioxidant activity, ***Research on Chemical Intermediates***, **49:** 4819-4843.
34. N. B. Tanaji, (2015) Determination of formation constants and thermodynamic parameters of trifluoperazine-metal complexes by potentiometric method, ***Der Pharma Chemica***, **7(6):** 59-63.
35. A. S. El-Tabl, F. A. El-Saied, A. N. Al-Hakimi, (2008) Spectroscopic characterization and biological activity of metal complexes with an ONO trifunctionalized hydrazone ligand, ***Journal of Coordination Chemistry***, **16(15)**: 2380-2401.
36. C. Xiao-Chun, T. Tao, W. Yin-Ge, P. Yu-Xin, H. Wei., Q. Hui-Fen, **(**2012) Azo-hydrazone tautomerism observed from UV-vis spectra by pH control and metal-ion complexation for two heterocyclic disperse yellow dyes. ***Dalton Transactions,*** **41(36):** 11107-11115.
37. K., M. Šumar, I. Ivanović-Burmazović, (2001) Thermal analysis in structural characterization of hydrazone ligands and their complexes, ***Journal of Thermal Analysis and Calorimetry***, **66:** 759-778.
38. F. M. Omar, F. Samy, (2021) Synthesis, spectral, thermal, potentiometric, antitumor, antimicrobial and PM3 studies of pyridazinone hydrazone metal complexes, ***Journal of Molecular Structure***, **1242:** 130744.
39. N. Narsimha, K. Sudeepa, M. Jaheer, M. Ravi, S. Sreekanth, C. Sarala Devi, (2018) Spectro analytical, computational and *in vitro* biological studies of novel substituted quinolone hydrazone and it's metal complexes, ***Journal of Fluorescence***, **28(1)**: 225-241.
40. G. Dongare, A. Aswar, (2021) Synthesis, spectral characterization, thermo-kinetic and biological studies of some complexes derived from tridentate hydrazone Schiff base, *Journal of Saudi Chemical Society*, 25(10): 101325.
41. B. R. Kirthan, M. C. Prabhakara, H. S. Bhojyanaik, P. H. Amith Nayak, R. Viswanath, H. B. Teja, Ereshanaika, (2022) Optoelectronic, photocatalytic, and DNA interaction studies of synthesised Cu(II), Co(II), and Ni(II) complexes containing schiff base Ligand, ***Inorganic Chemistry Communications***, **135:** 109109.
42. N. Chitrapriya, V. Mahalingam, M. Zeller, K. Natarajan, (2010) Synthesis, characterization, crystal structures and DNA binding studies of nickel(II) hydrazone complexes, *Inorganica Chimica Acta,* 363(14): 3685-3693.
43. Y. Li, Y. Zheng-Yin, W. Ming-Fang, (2010) Synthesis, characterization, DNA binding properties, fluorescence studies and antioxidant activity of transition metal complexes with hesperetin-2-hydroxy benzoyl hydrazone, ***Journal of Fluorescence***, **20(4):** 891-905.
44. a) N. H. Al-Sha'alan, (2007) Antimicrobial activity and spectral, magnetic and thermal studies of some transition metal complexes of a schiff base hydrazone containing a quinoline moiety, **Molecules**, **12(5):** 1080-1091. b) M. Yadav, S. Sharma, J. Devi, (2021) Designing, spectroscopic characterization, biological screening and antioxidant activity of mononuclear transition metal complexes of bidentate Schiff base hydrazones, ***Journal of Chemical Sciences*****, 133(21)**: 1-22.
45. S. Noreen, S. H. Sumrra, (2021) Aminothiazole-linked metal chelates: Synthesis, density functional theory, and antimicrobial studies with antioxidant correlations, *ACS Omega*, 6(48): 33085-33099.
46. E. A. Hassan, M. M. Ebrahium, A. M. Ebrahium, (2022) Metal complexes of hydrazone-oxime derivative as promising *in vitro* antimicrobial agents against some fungal and bacterial strains, ***Applied Organometallic Chemistry***, **36(5):** e6663.
47. M. Mohanraj, G. Ayyannan, G. Raja, C. Jayabalakrishnan, (2016) Synthesis, spectral characterization, DNA interaction, radical scavenging and cytotoxicity studies of ruthenium(II) hydrazone complexes, ***Journal of Photochemistry and Photobiology B: Biology***, **158:** 164-173.